DISCLAIMER

This report was prepared as an account of work sponsored by an agency of the United States Government. Neither the United States Government nor any agency thereof, nor any of their employees, makes any warranty, express or implied, or assumes any legal liability or responsibility for the accuracy, completeness, or usefulness of any information, apparatus, product, or process disclosed, or represents that its use would not infringe privately owned rights. Reference herein to any specific commercial product, process, or service by trade name, trademark, manufacturer, or otherwise does not necessarily constitute or imply its endorsement, recommendation, or favoring by the United States Government or any agency thereof. The views and opinions of authors expressed herein do not necessarily state or reflect those of the United States Government or any agency thereof. Reference herein to any social initiative (including but not limited to Diversity, Equity, and Inclusion (DEI); Community Benefits Plans (CBP); Justice 40; etc.) is made by the Author independent of any current requirement by the United States Government and does not constitute or imply endorsement, recommendation, or support by the United States Government or any agency thereof.

ORNL/TM-2025/4107

Report on Updated Properties Handbook of Printed Stainless Steel 316

Peeyush Nandwana
Selda Nayir
Caleb Massey
Geeta Kumari
David Collins
et al.

M2CR-22OR0402013

August 2025

ORNL/TM-2025/4107

Materials Science and Technology Division

REPORT ON UPDATED PROPERTIES HANDBOOK OF PRINTED STAINLESS STEEL 316

Peeyush Nandwana*
Selda Nayir*
Caleb Massey*
Geeta Kumari*
David Collins*
Mark Messner†
Xuan Zhang†
Michael McMurtrey‡
Robin A. Montoya§

* Oak Ridge National Laboratory
† Argonne National Laboratory
‡ Idaho National Laboratory
§ Los Alamos National Laboratory

M2CR-22OR0402013

August 2025

Prepared by
OAK RIDGE NATIONAL LABORATORY
Oak Ridge, TN 37831
managed by
UT-BATTELLE LLC
for the
US DEPARTMENT OF ENERGY
under contract DE-AC05-00OR22725

CONTENTS

LIST OF FIGURES

LIST OF TABLES

ABBREVIATIONS

AB	as-built
AM	additive manufacturing
AMMT	Advanced Materials and Manufacturing Technologies
ANL	Argonne National Laboratory
GE	General Electric
HIP	hot isostatic pressing
LANL	Los Alamos National Laboratory
LPBF	laser powder bed fusion
ORNL	Oak Ridge National Laboratory
SA	solution-annealed
SR	stress-relieved
SS	stainless steel
UTS	ultimate tensile strength
YS	yield strength

ABSTRACT

This report focuses on summarizing mechanical behavior of 316H stainless steel (SS) printed using laser powder bed fusion (LPBF). 316H SS is one of the six alloys that has been qualified for use in nuclear reactors. The Advanced Materials and Manufacturing Technologies (AMMT) program has identified the use of the additive manufacturing (AM) process of LPBF as one of the manufacturing modalities to fabricate components for nuclear applications. Unlike wrought material, AM material displays significant heterogeneity in properties, resulting from changes in process parameters, machine-to-machine variability, and minor changes in feedstock chemistry from one batch to another. Although significant work has been done on 316L SS in the literature and has been summarized in several review papers, very limited data exist on 316H SS. Therefore, this report aims to provide a concise summary of the properties of 316H SS printed using different machines and at different locations as a part of the AMMT program.

1. INTRODUCTION

The US Department of Energy Office of Nuclear Energy's AMMT program has identified LPBF as one of the AM technologies to be evaluated for its potential to fabricate high-quality, near net shape components for nuclear applications. The program's vision is to accelerate the development, qualification, and deployment of new materials and manufacturing technologies. 316H SS fabricated using LPBF was chosen to develop and demonstrate a rapid qualification pipeline. 316H SS was downselected owing to it being one of the six nuclear structural materials approved by the American Society of Mechanical Engineers *Boiler and Pressure Vessel Code*.

Commented [BR1]: Add to references

316L SS fabricated by LPBF has been extensively studied in terms of its microstructure and mechanical behavior [1–5]. However, limited studies exist on printed 316H SS, which is the higher-carbon variant (0.04–0.1 wt %) of 316 SS [6–8]. Most of the publicly available data on printed 316H SS have resulted from the AMMT program in terms of publicly available reports and publications in peer reviewed journals [9–15]. Within the AMMT program, printing and testing of 316H SS was undertaken as a collaborative effort between Oak Ridge National Laboratory (ORNL), Argonne National Laboratory (ANL), Los Alamos National Laboratory (LANL), and Idaho National Laboratory.

LPBF systems made by different OEMs can affect microstructure evolution because of the unique nuances of each system even if an attempt is made to use similar process parameters. Similarly, the powder feedstock, even when obtained from the same vendor, can have batch-to-batch variability that can affect material performance. These differences are the starkest in the as-printed condition, and the scatter in properties can be reduced via a host of postprocess treatments, such as hot isostatic pressing (HIP) and/or heat treatments. Therefore, the aim of this report is to first highlight the differences in material behavior originating from changes in OEMs or feedstock chemistry and subsequently provide the spread in data for eventual code case qualification and industry adoption of LPBF 316H SS. The data presented in this report were generated by this multilaboratory collaboration and pertain to tensile, creep, fracture, and fatigue behavior of the material. Creep–fatigue measurements are ongoing, and the data generated will be presented in future reports.

2. METHODOLOGY

Samples were printed on three different LPBF systems: the (1) General Electric (GE) Concept Laser M2 at ORNL, (2) Renishaw AM400 at ANL, and (3) EOS M290 at LANL. The 316H SS chemical composition specification is summarized in Table 1, along with the chemistries of the powders used for printing the coupons. Powder 1 (ORNL), Powder 2 (ANL), and Powder 3 (LANL) were used to conduct prints at ORNL, ANL, and LANL, respectively. The data generated to date are not sufficient to draw

statistical correlations about the effect of powder feedstock chemistry on the resulting material behavior. Because all powder compositions are within the range specified by the ASTM A240 specification [16], the difference in material behavior is attributed to changes in process parameters and the differences in the LPBF systems used in the program.

Table 1. Powder chemistries used to print 316H SS coupons tested in this study, along with the ASTM A240 specification. The compositions are in weight percent.

Element	ASTM A240 spec.	Powder 1 (ORNL)	Powder 2 (ANL)	Powder 3 (LANL)
Cr	16–18	17	16.8	16.7
Ni	10–14	12.3	12.1	11.9
Mo	2–3	2.3	2.5	2.6
Mn	<2	1.05	1.13	0.02
Si	<0.75	0.07	0.48	0.04
C	0.04–0.1	0.08	0.06	0.07
O	—	0.03	0.03	0.02
N	—	0.01	0.01	0.01
P	<0.045	<0.005	<0.005	<0.005
S	<0.03	0	0	0
Fe	Balance	Balance	Balance	Balance

The process parameters were developed and optimized for each machine and powder feedstock combination, with minimizing the porosity being the main aim. In situ process monitoring coupled with x-ray computed tomography was also used to aid process optimization on the GE Concept Laser M2. The details of process parameter development can be found elsewhere [9,17,18]. Test designs for subscale tensile and fracture toughness specimens and ASTM standard creep and fatigue specimens can be found elsewhere [11,13].

The data in this report are presented on samples tested in the following four conditions: (1) as-built (AB); (2) stress-relieved (SR) at 650°C for 24 h, followed by air cooling; (3) solution-annealed (SA) at 1,100°C for 1 h, followed by air cooling; and (4) HIP in the range of 1,120°C–1,163°C for 4 h at pressures greater than 100 MPa. Some samples were subjected to short- and long-term aging before testing, and those instances will be specified in the relevant sections of the report.

3. MICROSTRUCTURE

LPBF of 316H SS resulted in columnar grains regardless of the OEM system used to deposit the coupons [11,13]. The microstructure of 316H SS fabricated via LPBF was found to be very sensitive to the process parameters used, as shown in Figure 1 [19]. However, the dependence of microstructure on geometry has been reported to be minimal [13]. This was an important finding because it enabled the extraction of test coupons from different builds fabricated at the participating laboratories.

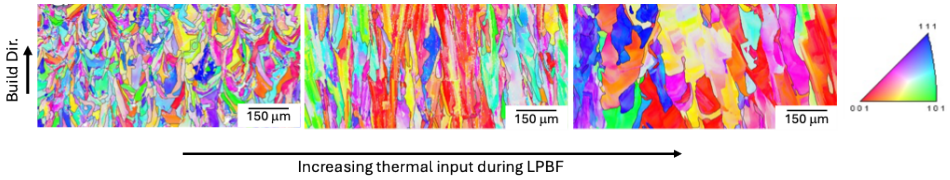

Figure 1. Sensitivity of 316H SS texture and grain size to thermal input during LPBF.

LPBF materials often encounter high residual stresses, which require SR heat treatments. Additionally, the highly textured and columnar microstructure can lead to anisotropy in material performance. As a result, the AMMT program also undertook efforts to postprocess the material via SA and HIP methods to determine if the printed 316H SS can be recrystallized [11,13,19]. Figure 2 shows the microstructure in AB, SR, SA, and HIP conditions. Postprocessing using standard conditions did not result in recrystallized grains. However, previous studies reported that the dislocation networks and solute segregation resulting from LPBF were annihilated and homogenized, respectively, during SA conditions (not shown here) [11].

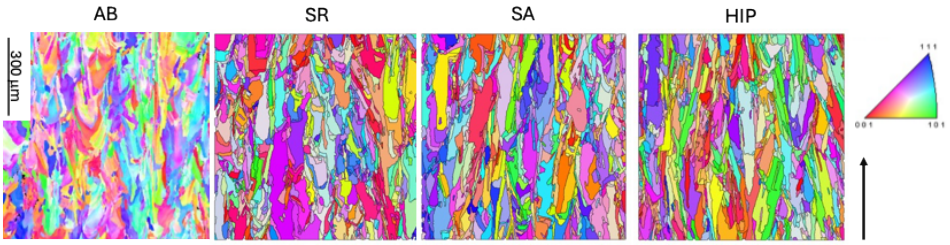

Figure 2. Columnar grains in AB, SR, SA, and HIP conditions.

4. TENSILE BEHAVIOR

Tensile testing was conducted on unaged samples fabricated at ORNL and ANL in AB, SR, SA, and HIP conditions to determine the anisotropy in material behavior and the influence of test temperature on the resulting tensile properties. However, because the components are expected to be subjected to elevated periods for prolonged time periods, a limited subset of samples fabricated at ANL in the AB condition were subjected to prolonged aging in the temperature range of 550°C–750°C for aging times ranging from 5 to 10,000 h. The following subsections present the property datasets for unaged and aged conditions.

4.1 TENSILE PROPERTIES OF UNAGED MATERIAL

The yield strength (YS), ultimate tensile strength (UTS), and elongation for ORNL and ANL builds are shown in Figure 3. The data were plotted to show the changes in tensile behavior as a function of temperature to reveal the variability in data, which resulted from the different LPBF OEMs used to deposit the builds, the test direction (i.e., along the build direction vs. transverse direction), and the effect of postprocessing. Notably, the plot does not account for the effect of process parameter changes for builds made on the same LPBF system. The effect of process parameters on resulting microstructure and performance heterogeneity was discussed in detail in the AMMT report, *Deposit and Evaluate Material Across Extremes of Process Windows* [19]. For the material deposited using the same LPBF system, the AB material had higher YS and UTS compared with the heat-treated conditions at all test temperatures. Some directional anisotropy was found in YS and UTS in the AB and SR conditions. However, SR and SA samples significantly reduced the anisotropy. In the heat-treated conditions, the tensile strength for similarly heat-treated samples was similar regardless of the LPBF system used for fabrication. With increasing tensile test temperature, YS and UTS generally reduced regardless of heat treatment or the LPBF system used. Elongation showed a higher scatter overall, making it more difficult to discern specific trends; the scatter could be attributed to porosity during LPBF as well as the effects of using a subscale sample. A previous study showed that sample size did not have a significant effect on YS and UTS but can influence total elongation [20].

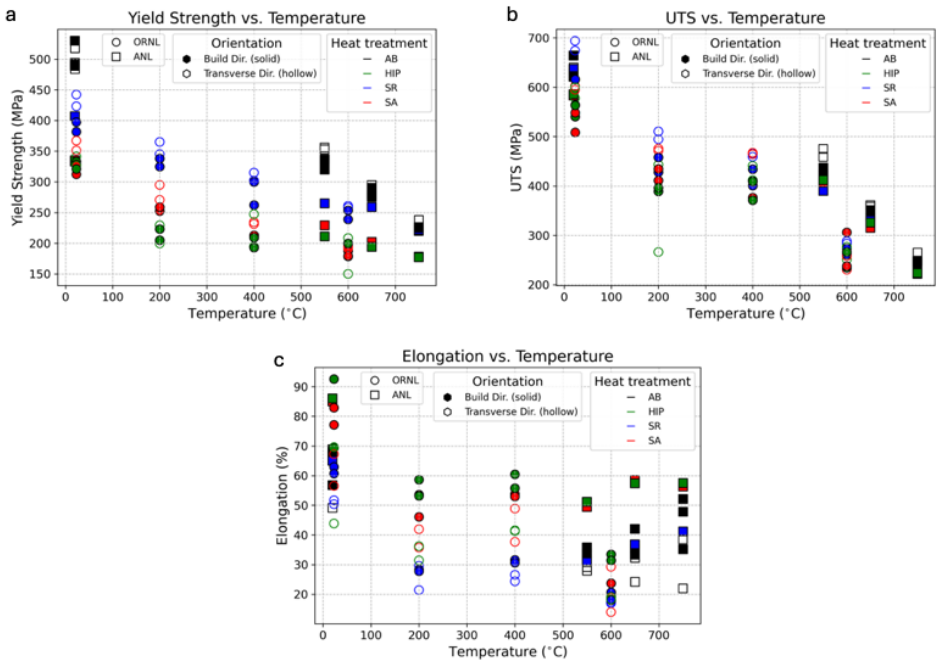

Figure 3. YS, UTS, and elongation of ORNL and ANL builds as a function of tensile test temperature, showing the effect of OEM, tensile test direction, and heat treatment.

In a production scenario, a variety of LPBF systems can be used depending on the vendor fabricating the parts. Data along the build and transverse directions also provide the bounds of tensile properties, especially as they pertain to complex parts. Therefore, to make the data agnostic to OEM and directional anisotropy for broad applicability, Figure 4 presents average values of YS and UTS as a function of postprocessing and tensile test temperature. On average, the YS of AB material was the highest, followed by SR, SA, and HIP, which had similar YS values. The reduction in YS from the SR condition is likely a result of annihilation of dislocation networks within the cells at this condition, but the cellular structure was retained in this condition [15]. Alternatively, HIP and SA resulted in dissociation of the cellular structure as well as homogenization of the material, which resulted in these two conditions having the lowest YS. Similar trends were observed for UTS (i.e., a reduction in UTS with increasing test temperature). However, the effect of different heat treatments was not as pronounced, which indicated differences in strain hardening between SR and HIP/SA conditions. Notably, some of the trends in data could be skewed because of different test temperatures chosen at ORNL and ANL. ORNL samples were tested at 200°C, 400°C, and 600°C, whereas high-temperature testing at ANL was conducted at 550°C, 650°C, and 750°C.

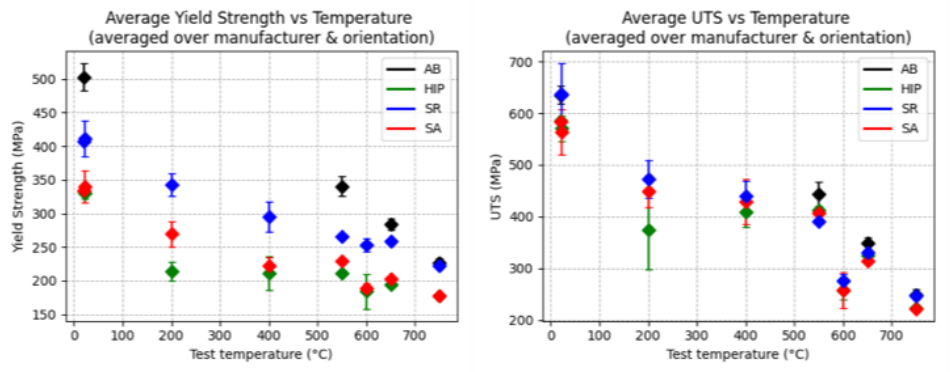

Figure 4. YS and UTS averaged over LPBF system manufacturer and orientation of the test specimen as a function of postprocessing and tensile test temperature.

Because the high-temperature tensile testing was conducted at different temperatures at ORNL and ANL, the change in YS and UTS as a function of temperature was parsed separately, and no distinction was made between the test orientation owing to the relatively minor anisotropy in tensile strength. Figure 5 shows the YS and UTS from ORNL and ANL builds with a linear fit to highlight that the relative drop in YS and UTS as a function of test temperature was similar for both cases. Therefore, the variation noted in the average YS and UTS was an artifact of the different test temperatures chosen.

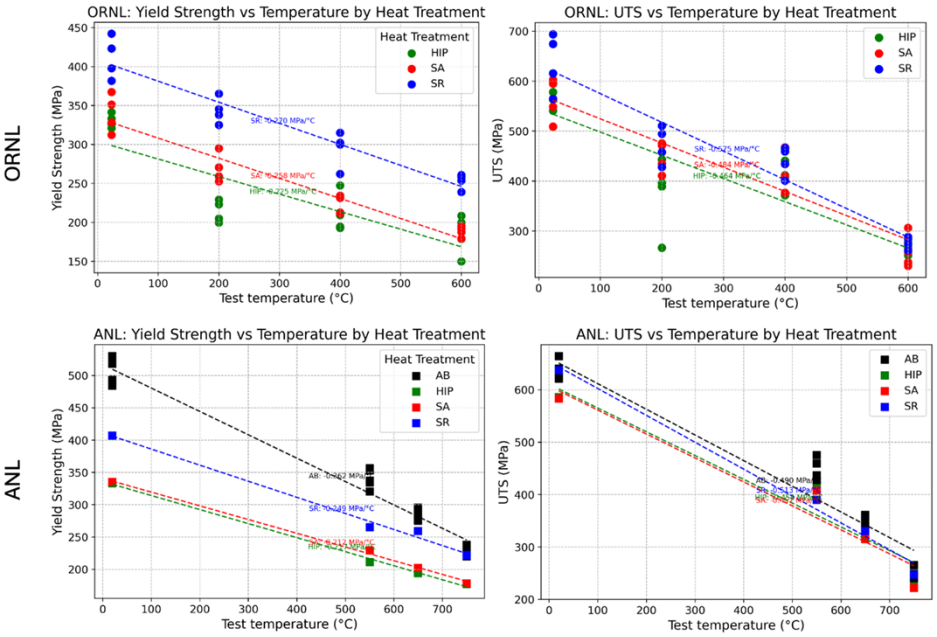

Figure 5. Linear fit showing similar trends in the reduction of (left) YS and (right) UTS as a function of temperature for samples fabricated at (top) ORNL and (bottom) ANL.

Commented [SN2]: Hard to read, needs high resolution plots

4.2 TENSILE PROPERTIES OF AGED MATERIAL

Figure 6 shows YS and UTS of the aged 316H SS. AB material deposited at ANL was subjected to aging at 550°C, 650°C, and 750°C. Tensile testing was conducted at the same temperature at which the sample was aged. This approach allowed determination of changes in tensile strength with aging times at different service conditions. Similar to unaged samples, the directional anisotropy was relatively low. The YS and UTS did not change significantly with time up to 10,000 h at 550°C and 650°C. At 750°C, YS showed a reduction beginning at 500 h of exposure and continued to drop thereon. UTS began to drop at 2,500 h.

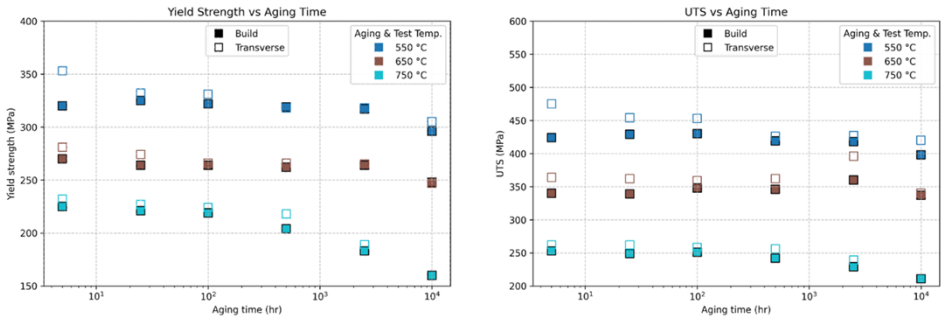

Figure 6. YS and UTS of aged 316H SS fabricated at ANL.

5. CREEP PERFORMANCE

The creep rupture data generated in the AMMT program to date is summarized in Figure 7. This figure shows summarized data based on the builds fabricated at ORNL, ANL, and LANL, and a distinction was not made based on the equipment used to fabricate the samples. Creep rupture tests were conducted at 600°C and 248 MPa, 725°C and 100 MPa, and 800°C and 53 MPa in AB, SR, SA, and HIP conditions. At 600°C, all samples failed within 500 h. More scatter in rupture times occurred during testing at 725°C and 800°C. At 800°C, almost all samples had very low creep ductility or strain at failure, with an average longer creep rupture life. On average at 725°C and 800°C, SR, SA, and HIP conditions result in longer creep rupture times compared with the AB condition.

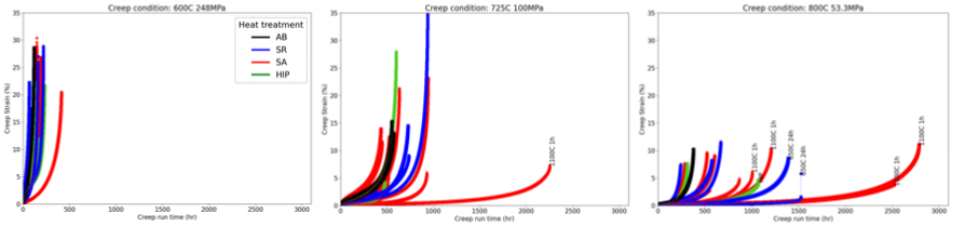

Figure 7. Creep performance of material at three different temperature–stress combinations.

Figure 8(a) shows significant scatter in creep ductility and rupture time, and no clear trends emerged in the data. Figure 8(b) shows that almost all samples tested at 600°C had creep elongation greater than 10%, whereas at 725°C, only the AB and SR samples had creep ductility lower than 10%. This result can potentially be attributed to the precipitation of embrittling sigma and Laves phases in the interdendritic region. AB samples have been shown to form Laves phase at 725°C within the first 100 h [19]. Interestingly, the creep ductility significantly dropped at 800°C regardless of the machine used to build the sample or the postprocessing treatment. Typically, over 10% ductility is desired to qualify the material for use in reactor applications [12]. Notably, at 600°C, SR samples had higher creep elongation even compared with the HIP condition, which could possibly indicate the influence of microstructure evolution on dominating failure; HIP is expected to close the AM porosity and densify the material. At 725°C, the HIP and SA conditions for ORNL samples displayed high creep ductility, and the ORNL samples in general displayed high creep ductility. The minimum creep rate between the different samples and

postprocess conditions was the largest for samples subjected to creep rupture testing at 600°C, as shown in Figure 8(c), with the ANL HIP and SA samples having the highest values for minimum creep rate. With increasing test temperature, the scatter in the minimum creep rate significantly reduced.

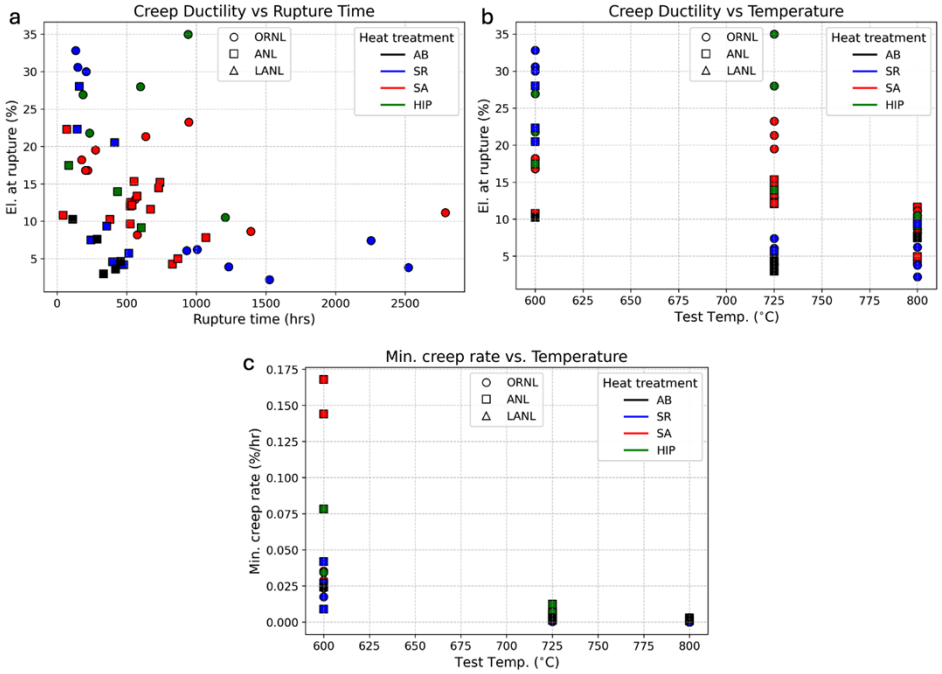

Figure 8. (a) Creep ductility vs. rupture time, (b) creep ductility vs. temperature, and (c) minimum creep rate vs. temperature.

Figure 9 shows the Larson–Miller parameters for the samples tested in the AMMT program calculated using the value of $C = 16.28$. At the measured stresses and temperatures, the data are comparable with wrought material. The comparison between wrought material and the data presented here can be found in [12].

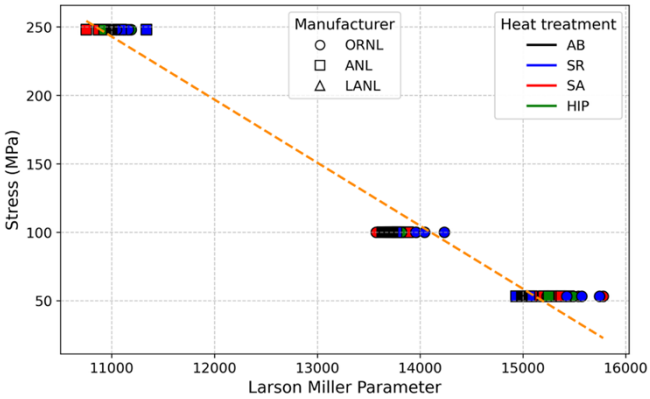

Figure 9. Creep rupture data collected to date displayed on a Larson–Miller diagram.

6. FRACTURE TOUGHNESS

Fracture toughness testing was conducted only on the samples produced at ORNL using the GE Concept Laser M2 system. Samples produced with two different energy density values (i.e., combinations of power, velocity, and hatch spacing) were tested. The individual data can be found elsewhere [13]. In Figure 10, the data have been averaged over the process parameter space to show the scatter. This is especially important in the case of complex geometries; even when using the same process parameter set, the thermal input can vary significantly depending on the cross section thickness. Notably, at all temperatures, the HIP condition resulted in the highest fracture toughness because of porosity closure. Porosity was expected to be present in AB, SR, and SA conditions and varied between the builds depending on the process variables used during fabrication. Interestingly, the SR sample had lower toughness than the AB condition at all test temperatures, and despite the scatter, the toughness of the AB material appeared to increase in the temperature range of 300°C–500°C. These differences correlate the superior combination of strength and ductility for AB samples compared with SR samples. However, detailed studies should be conducted to determine the evolution of microstructure with thermal exposure at different temperatures. Also, the data produced on subsize specimens should be validated against full-size ASTM samples, and this work will be undertaken in the future.

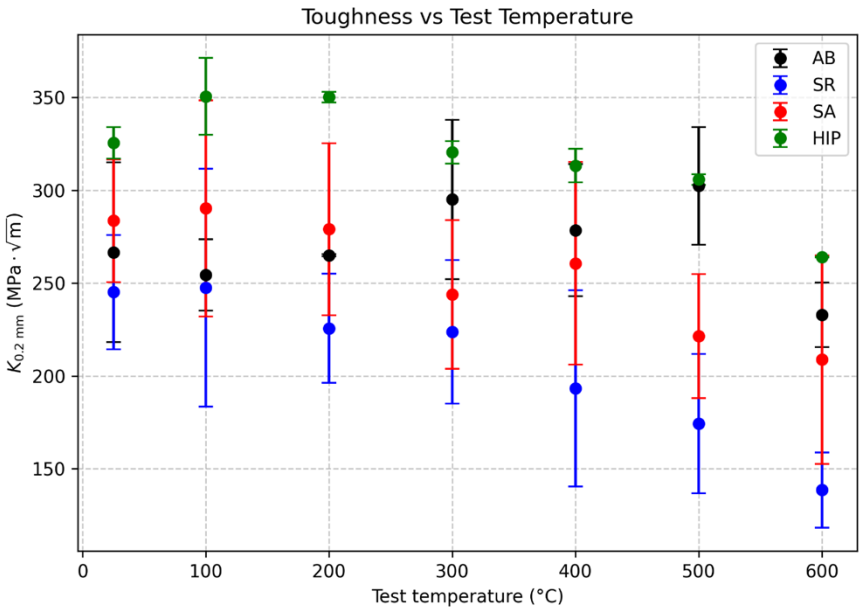

Figure 10. Fracture toughness data on samples produced using GE Concept Laser M2 at ORNL.

7. FATIGUE

Limited fatigue testing has been conducted within the program, and the most consistent data have been generated on ORNL and ANL samples that were subjected to fatigue testing at 550°C at $R = -1$. The fatigue plot is shown in Figure 11. At higher strain, the ORNL specimens displayed a higher number of cycles to failure, with SR, SA, and HIP conditions displaying similar cycles to failure; however, the ANL sample subjected to SA failed at the lowest number of cycles. More replicates should be tested to generate a statistically relevant dataset.

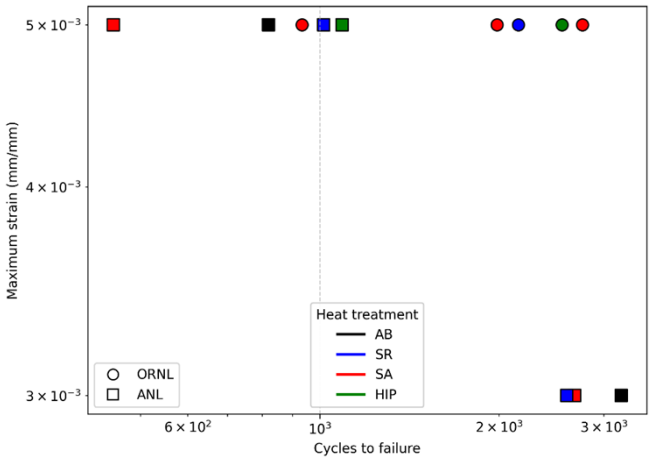

Figure 11. Fatigue behavior at 550°C for ORNL and ANL samples.

8. ONGOING EFFORTS

The multilab teams are planning to undertake longer-term creep tests, conduct creep–fatigue tests, and pinpoint the drivers of critical material properties. This handbook will be updated as new data are generated. In parallel, systematic efforts are being undertaken to determine the recrystallization kinetics during SA and the factors that influence recrystallization, such as AB microstructure or powder feedstock chemistry. Figure 12 shows that 316H SS fabricated at ORNL showed approximately 20%–30% recrystallized grains when subjected to solution annealing at 1,200°C for 1 h. Increasing the annealing time to 8 h resulted in no recrystallization at 1,000°C, approximately 20%–30% recrystallized grains at 1,100°C, and approximately 60%–70% recrystallized grains at 1,200°C. In contrast, 316H SS fabricated using the Renishaw AM400 at ANL showed complete recrystallization at 1,200°C and 4 h [11].

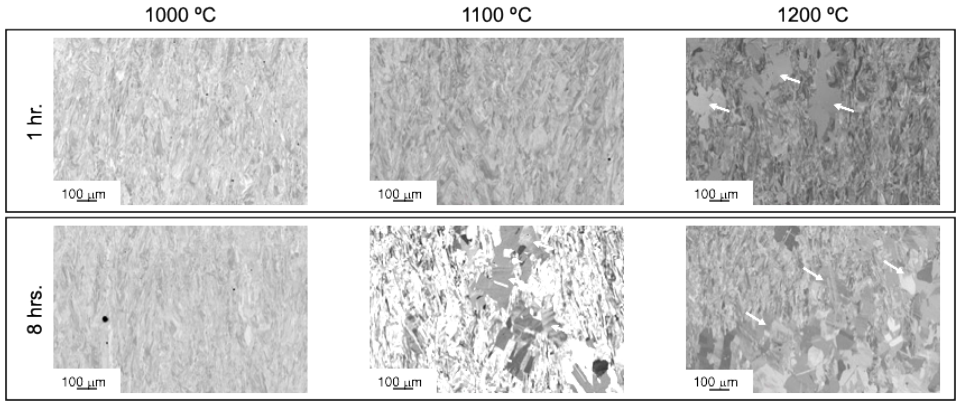

Figure 12. Sluggish recrystallization kinetics of 316H SS fabricated using GE Concept Laser M2 at ORNL.

9. SUMMARY AND OUTLOOK

The data presented in this report provide the range and scatter in different material properties in coupons fabricated using LPBF systems manufactured by different OEMs. Notably, process–parameter optimization was conducted with a focus on reducing porosity. Low creep ductility is a challenge, and during the AMMT program so far, it has been attributed to the formation of embrittling sigma and Laves phases. The accelerated kinetics of these phases results from solute segregation during LPBF. Therefore, a multidimensional approach is needed for process parameter optimization such that a combination of high density and low to minimal solute segregation is achievable. Furthermore, there is a critical need to understand the microstructure and feedstock chemistry drivers that influence the recrystallization kinetics during SA and HIP conditions to tailor the material performance and obtain predictable properties.

10. REFERENCES

[1] Y.M. Wang, T. Voisin, J.T. McKeown, J. Ye, N.P. Calta, Z. Li, Z. Zeng, Y. Zhang, W. Chen, T.T. Roehling, R.T. Ott, M.K. Santala, P.J. Depond, M.J. Matthews, A.V. Hamza, T. Zhu, Additively manufactured hierarchical stainless steels with high strength and ductility, Nat. Mater. 17 (2018) 63–71. https://doi.org/10.1038/nmat5021.

[2] T. Voisin, J.-B. Forien, A. Perron, S. Aubry, N. Bertin, A. Samanta, A. Baker, Y.M. Wang, New insights on cellular structures strengthening mechanisms and thermal stability of an austenitic stainless steel fabricated by laser powder-bed-fusion, Acta Mater. 203 (2021) 116476–116476. https://doi.org/10.1016/j.actamat.2020.11.018.

[3] S. Li, J. Hu, W.-Y. Chen, J. Yu, M. Li, Y. Wang, Evolution of cellular dislocation structures and defects in additively manufactured austenitic stainless steel under ion irradiation, Scr. Mater. 178 (2020) 245–250. https://doi.org/10.1016/j.scriptamat.2019.11.036.

[4] M. Li, W.-Y. Chen, X. Zhang, Effect of heat treatment on creep behavior of 316 L stainless steel manufactured by laser powder bed fusion, J. Nucl. Mater. 559 (2022) 153469. https://doi.org/10.1016/j.jnucmat.2021.153469.

[5] D. D'Andrea, Additive Manufacturing of AISI 316L Stainless Steel: A Review, Metals 13 (2023) 1370. https://doi.org/10.3390/ met13081370.

[6] B. Sutton, Assessment of 316H Stainless Steel Produced by Directed Energy Deposition Additive Manufacturing for High Temperature Power Plant Applications, in: Proc. Tenth Int. Conf., ASM International, Bonita Springs, Florida, USA, 2024: pp. 1020–1032. https://doi.org/10.31399/asm.cp.am-epri-2024p1020.

[7] M.A. Mahrous, M.A. Abdelghany, H. Farag, I. Jasiuk, Irradiation effects on additively manufactured porous 316H stainless steel: A molecular dynamics study, Comput. Mater. Sci. 258 (2025) 113985. https://doi.org/10.1016/j.commatsci.2025.113985.

[8] J. Snitzer, B. Wei, J. Shingledecker, J. Wang, X. Lou, High-temperature creep of additively manufactured 316H stainless steel by high-throughput microstructurally graded specimen: the effects of process and microstructure, Mater. Sci. Eng. A 943 (2025) 148750. https://doi.org/10.1016/j.msea.2025.148750.

[9] X. Zhang, S.A. Mantri, G.I. Vukovic, J. Listwan, D. Rink, E. Listwan, Development of process parameters and post-build conditions for qualification of LPBF 316 SS, 2023.

[10] X. Zhang, Y. Chen, S.A. Mantri, L. Gao, E. Listwan, J. Listwan, M. McMurtery, N. Mohale, C. Massey, FY24 Integrated Results for High-Temperature Mechanical Testing of LPBF 316H Stainless Steel, 2024.

[11] X. Zhang, L. Gao, S.A. Mantri, Technical basis for understanding the processmicrostructure-property correlation in LPBF 316 SS, 2024.

[12] M.C. Messner, X. Zhang, Y. Chen, C. Massey, M. McMurtrey, R.A. Montoya, M.J. Brand, O.R. Mireles, K. Le, Updated ASME design correlations and qualification plan for powder bed fusion 316H stainless steel, 2024.
[13] C. Massey, P. Nandwana, H. Hyer, S. Nayir, G. Kumari, J. Kendall, C. Joslin, D. Collins, T.G. Seibert, A. Godfrey, A.M. Rossy, A. Ziabari, Process–Property–Performance Mapping of Additively Manufactured 316H Stainless Steel Components, 2024.
[14] P. Nandwana, R. Kannan, S. Nayir, C. Massey, C. Joslin, PRELIMINARY REPORT ON COMPOSITIONAL SPECIFICATION FOR PRINTED 316SS, 2023.
[15] G. Kumari, T. Graening, X. Zhang, P. Nandwana, S. Nayir, S. Taller, C. Joslin, A.L. Musgrove, A. Godfrey, C. Massey, Post-build stress-relief optimization for laser powder bed fusion 316H stainless steel, Materialia 43 (2025) 102520. https://doi.org/10.1016/j.mtla.2025.102520.
[16] Standard Specification for Chromium and Chromium-Nickel Stainless Steel Plate, Sheet, and Strip for Pressure Vessels and for General Applications, 2004. https://doi.org/10.1520/A0240_A0240M-22.
[17] C. Massey, P. Nandwana, H. Hyer, S. Nayir, J. Kendall, C. Joslin, R. Duncan, D. Collins, T. Graening, L. Scime, Z. Snow, A. Ziabari, T. Butcher, R. Dehoff, DATA-DRIVEN OPTIMIZATION OF THE PROCESSING WINDOW FOR 316H COMPONENTS FABRICATED USING LASER POWDER BED FUSION, 2023.
[18] R. Montoya, M. Brand, K. Le, P. Beck, C. Giese, N. Barta, R. Bloom, C. Massey, X. Zhang, Process understanding for qualifying LPBF LH SS, 2023.
[19] P. Nandwana, S. Dryepondt, C. Massey, S. Bell, S. Nayir, G. Kumari, C. Joslin, DEPOSIT AND EVALUATE MATERIAL ACROSS EXTREMES OF PROCESS WINDOWS, 2025.
[20] R. Montoya, M. Brand, K. Le, M. Hayne, P. Beck, N. Barta, R. Bloom, J. Goodrich, J. Carpenter, A. Mirabel, M. Martinez, J. Stull, N. Debardelden, S. Chakrabarti, Advanced Materials & Manufacturing Technology (AMMT) Development of Additive Manufacturing Agnostic Process Parameter Procedure, 316H Stainless Steel Readiness Level Data Sets, and Machine Maintenance Plan, 2024.